



Cite this: *Nanoscale Adv.*, 2021, **3**, 2261

Enhanced oxygen reduction reaction activity and durability of Pt nanoparticles deposited on graphene-coated alumina nanofibres†

Sajid Hussain,^a Nadezda Kongi,^a Alexey Treshchalov,^b Tauno Kahro,^b Mihkel Rähn,^b Maito Merisalu,^b Aile Tamm,^b Väino Sammelselg^b and Kaido Tammeveski ^a

The oxygen reduction reaction (ORR) activity and stability of Pt catalysts deposited on graphene-coated alumina nanofibres (GCNFs) were investigated. The GCNFs were fabricated by catalyst-free chemical vapour deposition. Pt nanoparticles (NPs) were deposited on the nanofibres by sonoelectrochemical and plasma-assisted synthesis methods. Scanning and transmission electron microscopy analyses revealed different surface morphologies of the prepared Pt catalysts, depending on the synthesis procedure. Sonoelectrochemical deposition resulted in a uniform distribution of smaller Pt NPs on the support surface, while plasma-assisted synthesis, along with well-dispersed smaller Pt NPs, led to particle agglomeration at certain nucleation sites. Further details about the surface features were obtained from cyclic voltammetry and CO stripping experiments in 0.1 M HClO_4 solution. Rotating disk electrode investigations revealed that the Pt/GCNF catalyst is more active towards the ORR in acid media than the commercial Pt/C (20 wt%). The prepared catalyst also showed significantly higher durability than commercial Pt/C, with no change in the half-wave potential after 10 000 potential cycles.

Received 4th January 2021
Accepted 19th January 2021

DOI: 10.1039/d1na00007a
rsc.li/nanoscale-advances

Introduction

The oxygen reduction reaction (ORR) at the proton exchange membrane fuel cell (PEMFC) cathode is one of the few most important electrochemical reactions for eco-friendly renewable energy conversion.^{1–3} Pt-based electrocatalysts were extensively investigated for the ORR in the past few decades due to their considerably high electrocatalytic activity.^{4,5} However, the sluggish kinetics of the ORR and degradation of the supported Pt nanoparticles (NPs) under fuel cell operating conditions obstruct the large-scale commercialisation of PEMFC technology. Recent studies conclude that the synthesis procedure, defining both particle size distribution and anchoring mechanism of the Pt NPs, and the physicochemical nature of the support play key roles in the electrocatalytic activity and durability of Pt-based ORR catalysts.⁶ Besides, the crystallographic structures of the catalyst nanoparticles associated with specific adsorption energies define the kinetics of the ORR on the Pt surface.⁷ Consequently, various Pt deposition techniques and a variety of support materials are employed to fabricate more active and durable ORR electrocatalysts.^{8–14}

Carbon-based supports are usually preferred for this purpose due to their higher specific surface area, remarkable electrical conductivity, high chemical stability, and good mechanical and thermal resistance.^{15–17} However, carbon corrosion in the fuel cell environment is a serious drawback of using such supports because it compromises the durability of the cathode catalyst.^{18,19} Researchers have demonstrated that the nature of the carbon material plays an important role in improving the corrosion-resistance properties of the support.¹⁵ It has been revealed that graphene-based supports are more resistant to degradation due to their high graphitic features.²⁰ 2D graphene nanosheets are also preferred for a better distribution of catalyst nanoparticles because of their higher specific surface area compared to commercial amorphous carbon.²¹ Many studies indicate that functionalisation of the pristine graphene surface results in a better distribution of Pt nanoparticles and higher electrocatalytic activity of the cathode catalyst.^{22–27} Electronic interaction studies of Pt NPs with sp^3 and sp^2 carbon nanodomains revealed that the Pt NPs are more firmly attached to the sp^2 nanodomains.²⁸ Hussainova *et al.* investigated the surface composition of graphene layers prepared by chemical vapour deposition (CVD) on alumina nanofibres.²⁹ X-ray photoelectron spectroscopy (XPS) analysis showed that the graphene nanosheets completely cover the alumina surface, whereas approximately 75% of the carbon was sp^2 hybridised. Theoretically, sp^2 bonded carbon atoms in graphene layers are favourable active sites for the reduction of Pt^{4+} cations from the precursor solution, resulting in stronger attachment of the Pt

^aInstitute of Chemistry, University of Tartu, Ravila 14a, 50411 Tartu, Estonia. E-mail: kaido.tammeveski@ut.ee; Tel: +372 7375168

^bInstitute of Physics, University of Tartu, W. Ostwald Str. 1, 50411 Tartu, Estonia

† Electronic supplementary information (ESI) available. See DOI: [10.1039/d1na00007a](https://doi.org/10.1039/d1na00007a)



NPs to the support. Xiong and co-workers introduced a platinum-graphene hybrid nanostructure, prepared by a chemical method, as an excellent ORR catalyst in acid media.³⁰ The mass and specific activities for O₂ electroreduction of the prepared catalysts were 5.7 times and 7.0 times higher than those of the commercial Pt/C (40 wt%, E-TEK), respectively. Shao *et al.* deposited Pt on graphene nanoplates by ethylene glycol method.³¹ Stability measurements in 0.5 M H₂SO₄ showed that the Pt NPs deposited on graphene nanoplates were more resistant to degradation than those deposited on carbon nanotubes and carbon black. It is well-known that a uniform distribution of Pt NPs with an optimum particle size is essential for obtaining high electrocatalytic ORR activity. Such catalysts are also more resistant to degradation due to the stronger interaction of the Pt NPs with the support. Therefore, it is necessary to employ (and optimise) a deposition method which results in a better particle size distribution on the support surface. In our previous work, we reported uniform distribution of Pt NPs on reduced graphene oxide (rGO) and nitrogen-doped rGO with a narrow particle size distribution, using a plasma-assisted synthesis procedure.¹² The prepared catalysts showed comparable ORR activity to commercial Pt/C (20 wt%) in both acid and alkaline media.

Herein, we demonstrate uniform decoration of graphene-coated alumina nanofibres (GCNF) by Pt NPs without surface functionalisation and/or doping. The graphitic layers enfolding the alumina nanofibres provide excellent support for the Pt NPs deposited by sonoelectrochemical and plasma-assisted methods. The electrocatalytic activity for the ORR and durability of the prepared Pt/GCNF catalysts are investigated in 0.1 M HClO₄ solution.

Experimental

Graphenation of alumina nanofibres

For the graphenation of alumina fibres, a simple one-step catalyst-free CVD process was followed, similar to that described before.²⁹ A small bundle of fibres was collected in a quartz boat and placed into a quartz tube furnace followed by annealing at 1000 °C for 3 min in air and then for 5 min in Ar (99.999%, Linde) at a flow rate of 50 sccm. Afterwards, the fibres were exposed to a mixture of 10% CH₄ (99.999%, Linde) in Ar with a flow rate of 30 sccm at 1000 °C for 1 h. As the final step of the CVD process, the Ar/CH₄ mixture was replaced with Ar gas followed by cooling down the oven to room temperature. The white nonconductive alumina fibres became greyish and conductive after the few-layer graphitic coating by CVD.

Synthesis of Pt/GCNF catalysts

Chloroplatinic acid (H₂PtCl₆) is a strong acid and PtCl₆²⁻ anions can form a variety of Pt chloroaqua and chlorohydroxo octahedral complexes.^{32,33} To minimise hydrolysis, the stock aqueous solution of 1 mM H₂PtCl₆ (pH 2.7) prepared by dissolving chloroplatinic acid (H₂PtCl₆·6H₂O, 99.95%, Alfa Aesar) in Milli-Q water (18.2 MΩ cm) was stored at 5 °C in the dark. The stock H₂PtCl₆ solution was diluted with water at room temperature to 0.1 mM (pH 3.7) just before the processing. 4 mL of this

diluted solution was mixed with small amounts of graphenated alumina nanofibres and placed into a sealed silica cell. The solution was deaerated by bubbling He gas with a flow rate of 100 sccm for 10 min before the synthesis. To minimise agglomeration and precipitation of the nanocomposites during the processing, intense agitation of the solution was arranged using a low-power (~1 W) ultrasonic (1.7 MHz) transducer.

Before the deposition of the fibre-supported Pt catalysts onto a glassy carbon (GC) electrode, the concentration of the as-prepared colloidal solution was increased by about 20 times by simple centrifugal enrichment (10 000g, 30 min) and washing several times with water to a neutral pH. Two methods were employed for the preparation of Pt/GCNF catalysts: plasma-assisted synthesis (PS) and sonoelectrochemical deposition (SD) (see the ESI†).

Physical characterisation of catalysts

The surface morphology of the catalyst material was studied with a Helios NanoLab™ 600 (FEI) scanning electron microscope (SEM), and the structure and composition of the Pt NPs on the nanofibres were studied with a high-resolution transmission electron microscope (HRTEM), a Titan 200 (FEI). The HRTEM images were taken in bright-field mode with a 1024 × 1024 pixel imaging matrix using 200 kV and a 0.1 nA electron probe. The samples for both TEM imaging and analysis were prepared as follows: a microdrop of diluted catalyst suspension in isopropyl alcohol was dropped onto a Lacey carbon film substrate supported by a 300 copper mesh (Agar Scientific Ltd) followed by drying in air for 20 min. Micro-Raman spectroscopy measurements in back-scattering geometry were performed using a Renishaw inVia spectrometer with a confocal microscope and 514.5 nm excitation wavelength from an Ar ion laser. The sample was deposited on a silicon wafer plate. To avoid laser induced overheating and photochemistry effects, the laser power density on the sample was restricted to 10³ W cm⁻².

X-ray photoelectron spectroscopy (XPS) measurements were performed under ultra-high vacuum conditions by using a Scienta SES-100 electron energy analyser. For excitation, non-monochromatic Mg K_α X-rays (1253.6 eV) from a twin anode X-ray source (Thermo XR3E2) were used. For the wide-scan spectrum, 0.5 eV energy step and 1 s collection time per step were used; for the detailed Pt4f spectrum, the following parameters were employed: energy step 0.1 eV, 1 s per step and the number of sweeps is 3. For XPS data analyses CasaXPS software was used.

Texture parameters were determined by N₂ physisorption at 77 K using a NOVAtouch LX2 instrument (Quantachrome Instruments). The BET surface area of the GCNF support was calculated from N₂ adsorption according to the BET theory in the *P/P*₀ range of 0.02–0.2.

Electrochemical measurements

Electrochemical experiments were performed in 0.1 M HClO₄ solution using a standard three-electrode configuration and an Autolab potentiostat/galvanostat PGSTAT30 (Metrohm Autolab, The Netherlands). A Pt wire and a reversible hydrogen electrode (RHE) were used as counter and reference electrodes,



respectively. Polished glassy carbon (GC) was employed as the working electrode, which was modified with the catalyst ink prepared in Milli-Q®. The Pt loading on the GC surface was 52 $\mu\text{g cm}^{-2}$. For the electrochemical characterisation of the catalysts, cyclic voltammograms were recorded in the potential range of 0.05–1.2 V at a potential scan rate (ν) of 50 mV s^{-1} . CO-oxidation experiments were carried out at 20 mV s^{-1} . The ORR activity of the prepared catalysts was studied using a rotating disk electrode (RDE) setup consisting of an EDI101 rotator and a CTV101 speed control unit (Radiometer). An accelerated durability test (ADT) was performed by measuring 10 000 cycles in the potential range of 0.6–1.2 V at 50 mV s^{-1} . The electrochemical results obtained were compared to those of a commercial Pt/C (E-TEK, 20 wt%) catalyst.

Results and discussion

Surface characterisation

Raman spectroscopy provides a quick and facile evaluation of carbon nanostructures. Fig. 1 shows the Raman spectrum of alumina nanofibres graphenated by the CVD method. The spectrum is similar to the one reported by Hussainova *et al.*²⁹ The G (1585 cm^{-1}) and D (1342 cm^{-1}) bands correspond to the stretching vibrations of the sp^2 carbon atoms and the defect-induced breathing mode of aromatic rings, respectively.³⁴ The 2D band (2680 cm^{-1}) is symmetry-allowed and appears in the second-order Raman spectra of crystalline graphite (without any kind of disorder).³⁵ The strong and narrow D, G and 2D bands suggest nano-crystallinity of the few-layer graphene and the formation of the edge-type defects along the length of the nanofibers. Few-layer graphene is clearly visible in the HRTEM image of the graphenated alumina nanofibres (see Fig. S1†).

Fig. 2a and b show the SEM and Fig. 2c and d display the HRTEM images of Pt/GCNF(SD) and Pt/GCNF(PS) catalysts, respectively. It could be observed that the two Pt deposition methods resulted in entirely different Pt particle size distributions and surface coverage of the same substrate.

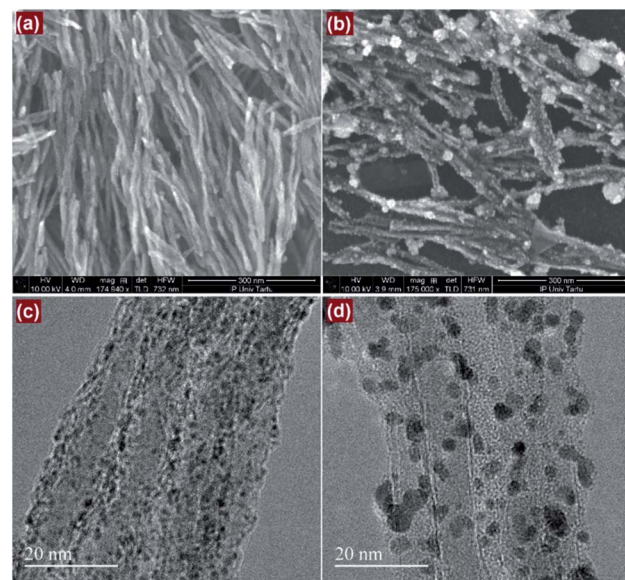


Fig. 2 SEM (a and b) and TEM (c and d) images of (a and c) Pt/GCNF(SD) and (b and d) Pt/GCNF(PS) samples, respectively.

In the case of SD, the nanofibres are uniformly decorated with quasi-spherical Pt nanoparticles with a diameter of about 1.3 nm, as presented in Fig. 2a and c. On the other hand, two types of Pt NPs were produced by PS; (i) smaller particles with a diameter of about 2.5 nm that homogeneously cover the support surface and (ii) larger, flower-like agglomerates of various sizes, ranging from 5 to 60 nm in diameter as presented in Fig. 2b and d. This could be related to the surface diffusion of the nuclei and/or different surface energies of the active sites. It can be predicted that the smaller NPs are electrochemically more active and resistant to degradation due to the stronger interaction with the graphene support. The ideal catalyst support for practical PEMFC application should present a micropore-free structure, with non-porous NPs dispersed on its surface.^{3,36} The main advantage of such a morphology is connected with the fact that ionomers cannot enter nanopores that are smaller than the Nafion® aggregates (e.g. less than 10 nm). In addition, the strong interfacial bonding between the catalyst particles and the support is crucial to prevent degradation of the catalyst material.³⁷ From this point of view the three-dimensional *meso*-structure offered by the interconnected network of conductive nanofibres decorated with small Pt NPs provides an ideal morphology for the electrochemical processes with improved charge (protons) and mass (oxygen) transport processes.

The chemical composition of the catalyst surface was analysed using X-ray photoelectron spectroscopy. Fig. 3 shows the XPS survey and high-resolution spectra in the Pt4f region for Pt/GCNF(SD) and Pt/GCNF(PS) catalysts. Survey spectra show the oxygen (O1s), carbon (C1s), platinum (Pt4f and Pt4d) and aluminium (Al2p and Al2s) peaks in both samples (see Fig. 3a). The presence of oxygen and aluminium can be attributed to the alumina support, while carbon and platinum peaks belong to the surface of catalysts. Due to the overlapping of Pt4f and Al2p XPS spectra the analysis of the

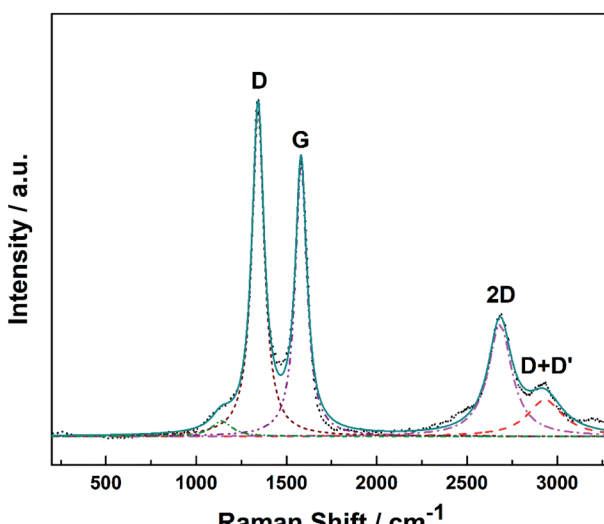


Fig. 1 Raman spectrum of alumina nanofibers graphenated by the CVD method.



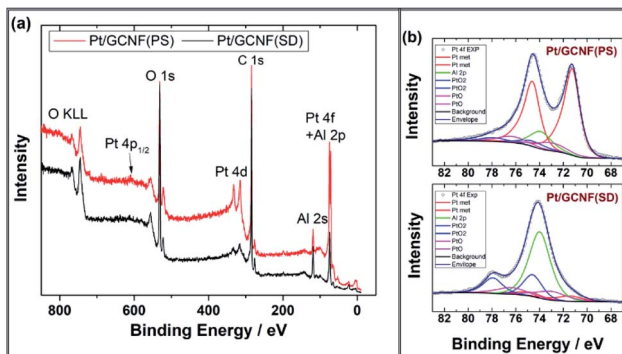


Fig. 3 (a) XPS survey spectra and (b) high-resolution spectra in the Pt4f region for Pt/GCNF(PS) and Pt/GCNF(SD) samples. Curve fitting was performed for the Pt4f peaks.

chemical state of platinum was performed using curve fitting. The intensity of the Al2p peak was adjusted by using the intensities of the Al2s peak. For the Pt4f_{7/2} peak, three components are taken into account: metallic Pt with a binding energy of 71.6 eV, PtO with a binding energy of 73.0 eV and PtO₂ with a binding energy of 74.6 eV, as presented in Fig. 3b.³⁸ For the Pt4f_{5/2} peak the binding energies are correspondingly 3.35 eV higher. The fitting results show that in the spectra of the as-prepared Pt/GCNF(PS) sample, the metallic Pt dominates, but in the case of Pt/GCNF(SD), PtO₂ dominates.

The BET surface area of the graphenated alumina nanofibre support determined from N₂ physisorption isotherms was found to be 215 m² g⁻¹, which is similar to that obtained in an earlier publication.³⁹

Electrochemical characterisation

Fig. 4a displays the normalised CO oxidation peaks of Pt/GCNF(SD) and Pt/GCNF(PS) catalysts in comparison to that obtained for the commercial Pt/C. It can be seen that all Pt catalysts under investigation exhibit different CO oxidation profiles. For instance, commercial Pt/C shows a typical single CO oxidation peak located at 0.79 V_{RHE}. Pt/GCNF(SD) shows a broad peak at 0.72 V_{RHE} and a shoulder at 0.80 V_{RHE}. We have previously reported such CO electro-oxidation behaviour of Pt deposited on different (sp² and sp³-like) carbon nanodomains.¹⁰ It has been demonstrated previously that the particle size and anchoring mechanism of the Pt NPs and the support effect play key roles in facilitating the electrooxidation of the adsorbed CO at the active sites.^{11,28,40} Interestingly, Pt/GCNF(PS) exhibits two distinct CO oxidation peaks at 0.71 and 0.80 V_{RHE}. A small plateau in the current density followed by a rapid increase can also be observed at 0.68–0.70 V_{RHE}. This CO oxidation behaviour is unusual, which could be attributed to the different nature and energies of the adsorption sites of the two types of nanoparticles seen in Fig. 2b and d associated with the support effect. Arenz *et al.* reported that the CO electro-oxidation peak shifts to lower potential with increasing Pt particle size.⁴¹ Hence, it can be concluded that the peak at 0.71 V_{RHE} is

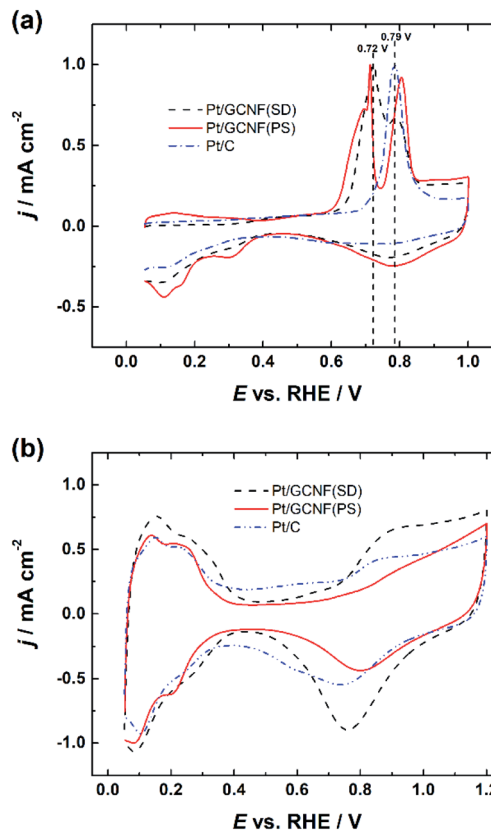


Fig. 4 Comparison of (a) normalised CO electro-oxidation peaks and (b) cyclic voltammograms of Pt/GCNF(SD), Pt/GCNF(PS) and Pt/C catalysts in 0.1 M HClO₄.

attributed to the bigger agglomerates while that at 0.80 V_{RHE} is attributed to the smaller Pt nanoparticles.

Cyclic voltammograms (CVs) were recorded in Ar-saturated 0.1 M HClO₄ solution after electrochemical cleaning of the Pt catalyst surface by CO stripping. The CV curves shown in Fig. 4b also confirm the size-dependent electrochemical properties of the Pt catalysts, see a comparison of the hydrogen adsorption/desorption peaks, double-layer capacitance and Pt-oxide formation and reduction peaks. These results are in good agreement with previous studies reported by Arenz *et al.*⁴¹

These results also confirm the reduction of the thermodynamically unstable oxides on Pt/GCNF(SD) (Fig. 3) in the region of potential cycling. The real surface area (A_r) of the Pt catalysts was determined from the hydrogen desorption peaks and the values are listed in Table 1. Pt/GCNF(SD) exhibits a 2 times higher surface area of 1.71 cm² than the commercial Pt/C (0.88 cm²), which can be expected from the uniformly distributed smaller nanoparticles on the graphene surface (Fig. 2a and c). Moreover, the surface area of Pt/GCNF(PS) is 44% higher than that of the commercial Pt/C, attributed to the porous nature of the flower-like Pt aggregates formed at the support surface.

Oxygen reduction reaction studies

RDE measurements in O₂-saturated 0.1 M HClO₄ solution reveal that both Pt/GCNF catalysts possess remarkable activity for the



Table 1 Kinetics parameters for the ORR on Pt/GCNF and commercial 20 wt% Pt/C catalysts in 0.1 M HClO₄

Electrode	A_r (cm ²)	$E_{1/2}$ (V _{RHE})	Tafel slope I ^a (mV)	Tafel slope II ^a (mV)	SA at 0.9 V (mA cm ⁻²)	MA at 0.9 V (A g ⁻¹)
Pt/GCNF(PS)	1.27	0.89	-61	-113	0.48	93
Pt/GCNF(SD)	1.71	0.88	-67	-127	0.27	70
Pt/C	0.88	0.87	-58	-111	0.40	55

^a Region I corresponds to low current densities and region II to high current densities.

electroreduction of oxygen in acid media. Fig. 5a and b show the ORR polarisation curves of Pt/GCNF(SD) and Pt/GCNF(PS) recorded at various rotation rates. The diffusion-limited current densities are in good agreement with the theoretical values of a 4-electron ORR process. The Koutecký–Levich (K–L) plots constructed on the basis of RDE data are presented in Fig. 5c and d. The insets in Fig. 5c and d indicate the number of electrons transferred (n) in the O₂ reduction, calculated using the K–L equation:

$$\frac{1}{j} = \frac{1}{j_k} + \frac{1}{j_d} = -\frac{1}{nFkC_{O_2}^b} - \frac{1}{0.62nFD_{O_2}^{2/3}\nu^{1/6}C_{O_2}^b\omega^{1/2}}, \quad (1)$$

where j is the measured current density, j_k is the kinetic current density, j_d denotes the diffusion-limited current density, F is the Faraday constant (96 485 C mol⁻¹), k is the rate constant for the electrochemical reduction of oxygen, $C_{O_2}^b$ is the concentration of O₂ in the solution (1.22 × 10⁻⁶ mol cm⁻³),⁴² D_{O_2} is the diffusion coefficient of O₂ (1.93 × 10⁻⁵ cm² s⁻¹),⁴² ν is the solution kinematic viscosity (0.01 cm² s⁻¹)⁴³ and ω is the electrode rotation speed (rad s⁻¹).

A comparison of the RDE polarisation curves at 1600 rpm is presented in Fig. 6a, which shows that the prepared Pt/GCNF catalysts exhibit comparable ORR electrocatalytic activity to

commercial Pt/C (20 wt%). The half-wave potential ($E_{1/2}$) values of Pt/GCNF(PS), Pt/GCNF(SD) and Pt/C were found to be 0.89, 0.88 and 0.87 V_{RHE}, respectively (see Table 1). These values are comparable to those reported by Maia and co-workers, where 80 µg cm⁻² Pt was electrochemically deposited on graphene nanoribbons (GNRs).⁴⁴ According to their study, the Pt catalyst electrodeposited on GNRs is more active and durable than that deposited on graphene oxide nanoribbons and carbon nanotubes. Liu *et al.* recently reported the $E_{1/2}$ of Pt deposited on N-doped carbon to be 0.88 V_{RHE} in 0.1 M HClO₄ solution.⁴⁵

Moreover, the Tafel plots for O₂ reduction presented in Fig. 6b are constructed on the basis of the RDE data obtained from Fig. 6a. The Tafel slope values determined at low and high

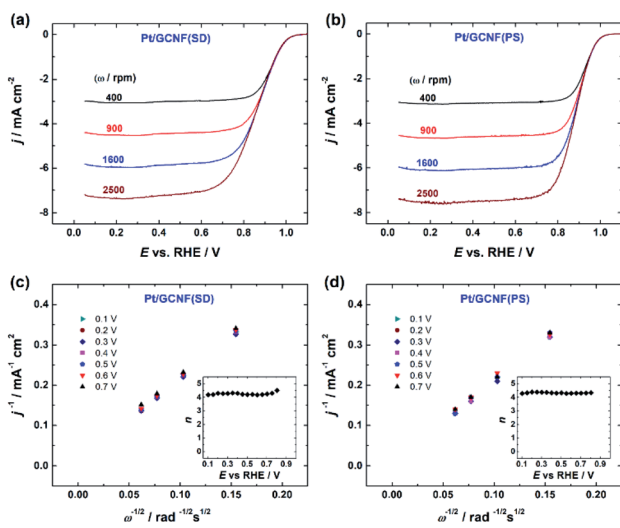


Fig. 5 RDE polarisation curves for oxygen reduction on (a) Pt/GCNF(SD) and (b) Pt/GCNF(PS) catalysts recorded in O₂-saturated 0.1 M HClO₄ at various rotation speeds ($\nu = 10$ mV s⁻¹); K–L plots of (c) Pt/GCNF(SD) and (d) Pt/GCNF(PS) catalysts. The insets to (c) and (d) indicate the 4-electron ORR pathway on both catalysts.

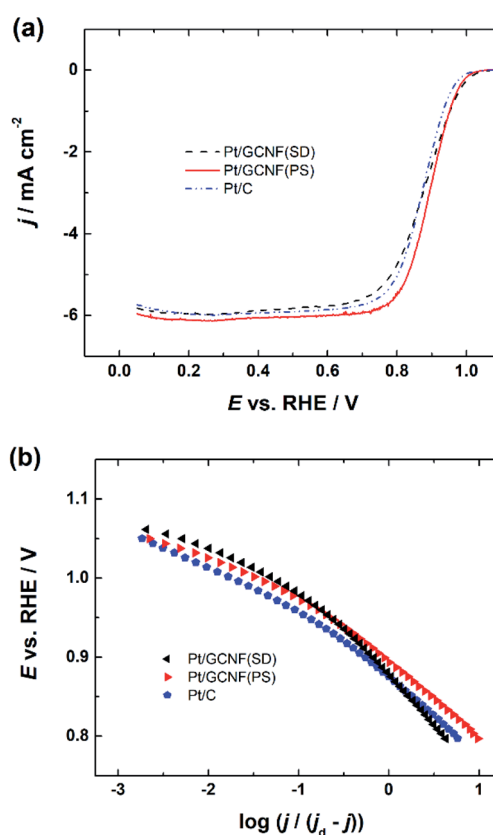


Fig. 6 (a) RDE polarisation curves for oxygen reduction on Pt/GCNF(PS), Pt/GCNF(SD) and Pt/C catalysts recorded in O₂-saturated 0.1 M HClO₄ solution at 1600 rpm and (b) Tafel plots for the ORR of the respective catalysts.



current density regions are close to -60 and -120 mV, indicating that the slow first electron transfer to O_2 is the rate-determining step.⁴⁴

Specific activity (SA) and mass activity (MA) values for O_2 reduction on the electrocatalysts were calculated at 0.9 V_{RHE} using the following equations:

$$SA = I_k/A_r \quad (2)$$

$$MA = I_k/m_{Pt} \quad (3)$$

where I_k is the kinetic current, A_r is the real surface area of Pt and m_{Pt} is the mass of Pt on the electrode surface.

As listed in Table 1, the Pt/GCNF(PS) showed the highest SA of 0.48 mA cm $^{-2}$ followed by Pt/C (0.40 mA cm $^{-2}$). Pt/GCNF(SD) showed a relatively low SA of 0.27 mA cm $^{-2}$, which can be ascribed to the smaller size of the deposited Pt NPs. These results are more promising than those of our previous investigations where Pt deposited on reduced graphene oxide and nitrogen-doped graphene oxide exhibited SA values of 0.20 and 0.22 mA cm $^{-2}$ in 0.05 M H₂SO₄, respectively.¹² The mass activities of Pt/GCNF(PS), Pt/GCNF(SD) and Pt/C catalysts were found to be 93 , 70 and 55 A g $^{-1}$. The specific and mass activities of Pt NPs electrodeposited on GNR are previously reported to be 0.67 mA cm $^{-2}$ and 104 A g $^{-1}$, respectively.⁴⁴ Erkey and co-workers chemically deposited Pt NPs on graphene aerogel (GA) synthesised by a modified Hummers method. The SA values (at 0.85 V_{RHE}) of the Pt/GA catalysts heated in a N₂ atmosphere at 400 , 600 and 800 °C were found to be 6.6 , 2.3 and 34.4 μ A cm $^{-2}$ and the MA values were 27.2 , 30.6 and 12.0 A g $^{-1}$, respectively.⁴⁶ The SA values of Pt decorated on rGO and pristine graphite were found to be 0.67 and 0.29 mA cm $^{-2}$, respectively.⁴⁷ The MA values of Pt/rGO and Pt/graphite were 92 and 42 A g $^{-1}$, respectively.

Accelerated durability test

Based on the smaller size of the deposited Pt nanoparticles, Pt/GCNF(SD) was chosen for the durability tests. Fig. 7 displays the CV curves, CO oxidation peaks and RDE polarisation curves of the Pt/GCNF(SD) catalyst in comparison to those of the commercial Pt/C, measured before and after $10\,000$ cycles in the potential range of 0.6 – 1.2 V_{RHE} at 50 mV s $^{-1}$. The real Pt surface area calculated from the hydrogen desorption peaks revealed that Pt/GCNF(SD) retains 83.5% of its surface area, while Pt/C retains only 44.3% (Fig. 7a). The trend in the surface area loss could also be observed in the CO oxidation peaks shown in Fig. 7b. Furthermore, no significant shift was observed in the $E_{1/2}$ of Pt/GCNF(SD) during the durability test, while that of the commercial Pt/C decreased by 36 mV.

Fig. 8 shows a decrease in the A_r , SA and MA values of the catalysts after the ADT. The SA of Pt/GCNF(SD) and Pt/C decreased by 0.025 and 0.029 mA cm $^{-2}$ and the MA decreased by 9.3 and 32.2 A g $^{-1}$, respectively. These results elucidate that Pt/GCNF(SD) is much more durable in acid media than commercial Pt/C.

The corrosion-resistance properties of graphene-based supports for Pt-based ORR catalysts have been recently

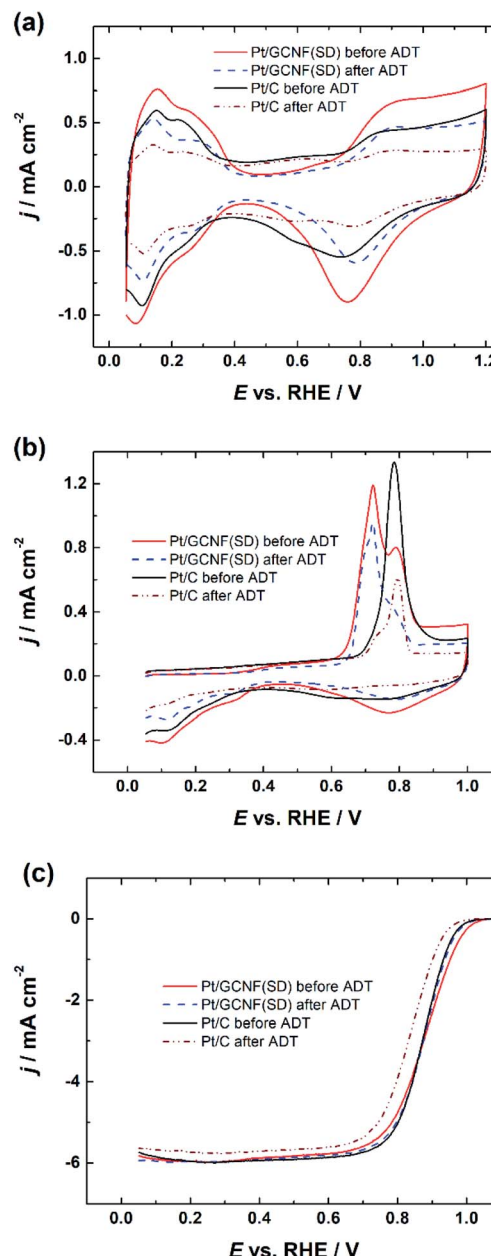


Fig. 7 (a) Cyclic voltammograms, (b) CO electro-oxidation and (c) RDE polarisation curves of Pt/GCNF(SD) and Pt/C catalysts recorded at 1600 rpm before and after the ADT.

reported by many groups.^{48–51} Huang and co-workers reported that Pt deposited on rGO retains 46% of its initial surface area after $20\,000$ potential cycles between 0.6 and 1.1 V_{RHE} in 0.1 M HClO₄ while commercial Pt/C retained $\sim 51\%$ of the initial surface area.⁵² Bertin *et al.*⁵³ recently demonstrated that Pt NPs deposited on graphene by pulse laser ablation are more resistant to degradation, retaining 75% of the initial surface area after the ADT. In comparison, Pt deposited on carbon black retained only 38% of its surface area.

Hussainova *et al.*²⁹ followed a different protocol for the durability test of Pt NPs deposited on graphene-coated alumina



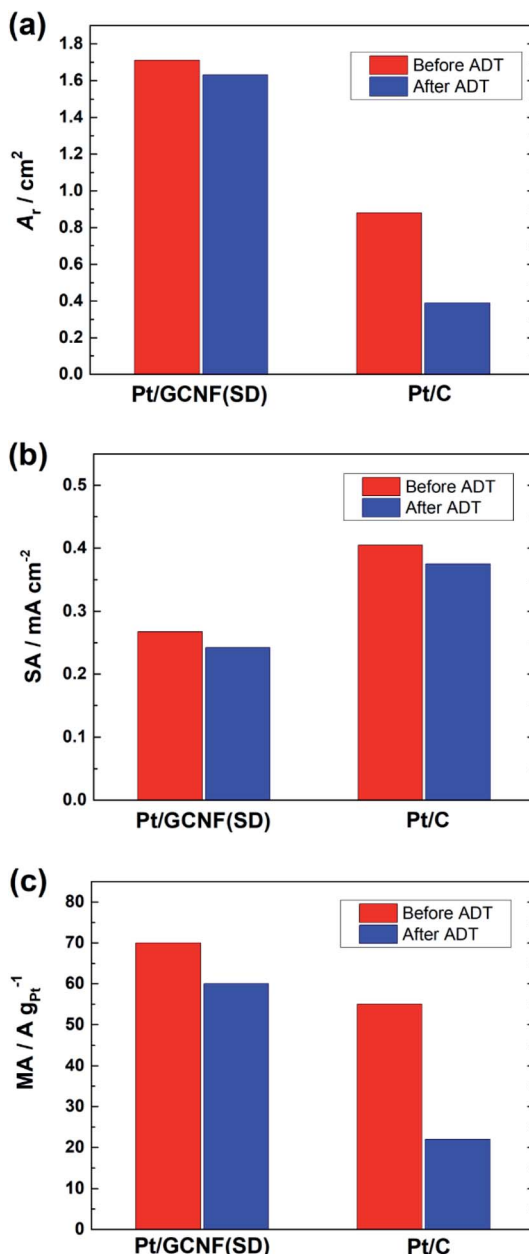


Fig. 8 (a) The real surface area, (b) specific activity (at 0.9 V_{RHE}) and (c) mass activity (at 0.9 V_{RHE}) of Pt/GCNF(SD) and Pt/C catalysts before and after the ADT.

nanofibres, where 30 000 potential scans were applied between 1.0 and 1.5 V_{RHE} at 500 mV s⁻¹. They reported a 3% decrease in the catalyst surface area after the ADT. In this work the high stability of Pt/GCNF(SD) can be attributed to the following phenomena.

- (i) Pt NPs deposited by the sonoelectrochemical method are more firmly attached to the graphene support surface.
- (ii) The smaller size of Pt NPs, which results in stronger interaction with the graphene support.
- (iii) Graphitic nature of the catalyst support, which is less corrosive under harsh electrochemical conditions.

Conclusions

Alumina nanofibres were completely coated with few-layered graphene using the CVD method. The SEM and TEM analysis and electrochemical characterisation revealed that the particle size distribution of Pt NPs and the surface electrochemistry of Pt/GCNF catalysts depend on the deposition method, *i.e.* plasma-assisted and sonoelectrochemical treatment in surfactant-free water solution. Both types of Pt/GCNF catalysts showed remarkable electrocatalytic activity towards the ORR in acid media, irrespective of the nature and size of the Pt NPs. Durability measurements confirmed that Pt NPs deposited by the sonoelectrochemical method are more durable than commercial Pt/C (20 wt%). The simple, one-step and easily scalable sonoelectrochemical method, demonstrated in this work, is very promising for the decoration of various conductive support surfaces by well-dispersed small metal NPs.

Conflicts of interest

There are no conflicts to declare.

Acknowledgements

This work was financially supported by the Estonian Research Council (grants PRG723, TLTFY14054T, and PRG4). This research was also supported by the EU through the European Regional Development Fund (TK141, “Advanced materials and high-technology devices for energy recuperation systems”, and TK134, “Emerging orders in quantum and nanomaterials”). We would like to thank Dr Maike Käärik (Institute of Chemistry, University of Tartu) for BET analysis and Dr Arvo Kikas (Institute of Physics, University of Tartu) for XPS analysis.

References

- 1 C. W. Wu, W. Zhang, X. Han, Y. X. Zhang and G. J. Ma, *J. Power Sources*, 2020, **476**, 228724.
- 2 I. Katsounaras, S. Cherevko, A. R. Zeradjanin and K. J. J. Mayrhofer, *Angew. Chem., Int. Ed.*, 2014, **53**, 102–121.
- 3 A. Ly, T. Asset and P. Atanassov, *J. Power Sources*, 2020, **478**, 228516.
- 4 X. Q. Wang, Z. J. Li, Y. T. Qu, T. W. Yuan, W. Y. Wang, Y. Wu and Y. D. Li, *Chem.*, 2019, **5**, 1486–1511.
- 5 S. Sui, X. Y. Wang, X. T. Zhou, Y. H. Su, S. Riffat and C. J. Liu, *J. Mater. Chem. A*, 2017, **5**, 1808–1825.
- 6 S. Hussain, H. Erikson, N. Kongi, A. Sarapuu, J. Solla-Gullón, G. Maia, A. M. Kannan, N. Alonso-Vante and K. Tammeveski, *Int. J. Hydrogen Energy*, 2020, **45**, 31775–31797.
- 7 J. C. Dong, M. Su, V. Briega-Martos, L. Li, J. B. Le, P. Radjenovic, X. S. Zhou, J. M. Feliu, Z. Q. Tian and J. F. Li, *J. Am. Chem. Soc.*, 2020, **142**, 715–719.
- 8 S. Hussain, H. Erikson, N. Kongi, A. Tarre, P. Ritslaid, M. Rähn, L. Matisen, M. Merisalu, V. Sammelselg and K. Tammeveski, *Int. J. Hydrogen Energy*, 2018, **43**, 4967–4977.



9 S. Hussain, H. Erikson, N. Kongi, M. Merisalu, M. Rähn, V. Sammelselg, G. Maia and K. Tammeveski, *J. Electrochem. Soc.*, 2017, **164**, F1014–F1021.

10 S. Hussain, N. Kongi, L. Matisen, J. Kozlova, V. Sammelselg and K. Tammeveski, *Electrochem. Commun.*, 2017, **81**, 79–83.

11 S. Hussain, N. Kongi, H. Erikson, M. Rähn, M. Merisalu, L. Matisen, P. Paiste, J. Aruväli, V. Sammelselg, L. A. Estudillo-Wong, K. Tammeveski and N. Alonso-Vante, *Electrochim. Acta*, 2019, **316**, 162–172.

12 S. Hussain, H. Erikson, N. Kongi, A. Treshchalov, M. Rähn, M. Kook, M. Merisalu, L. Matisen, V. Sammelselg and K. Tammeveski, *ChemElectroChem*, 2018, **5**, 2902–2911.

13 S. Hussain, H. Erikson, N. Kongi, A. Tarre, P. Ritslaid, A. Kikas, V. Kisand, J. Kozlova, J. Aarik, A. Tamm, V. Sammelselg and K. Tammeveski, *J. Electrochem. Soc.*, 2020, **167**, 164505.

14 D. Gohl, A. Garg, P. Paciok, K. J. J. Mayrhofer, M. Heggen, Y. Shao-Horn, R. E. Dunin-Borkowski, Y. Roman-Leshkov and M. Ledendecker, *Nat. Mater.*, 2020, **19**, 287–291.

15 P. Trogadas, T. F. Fuller and P. Strasser, *Carbon*, 2014, **75**, 5–42.

16 Y. Wang, J. Li and Z. D. Wei, *ChemElectroChem*, 2018, **5**, 1764–1774.

17 K. Singh, E. B. Tetteh, H. Y. Lee, T. H. Kang and J. S. Yu, *ACS Catal.*, 2019, **9**, 8622–8645.

18 X. Yu and S. Ye, *J. Power Sources*, 2007, **172**, 145–154.

19 H. Singh, S. Q. Zhuang, B. Ingis, B. B. Nunna and E. S. Lee, *Carbon*, 2019, **151**, 160–174.

20 D. Higgins, P. Zamani, A. Yu and Z. Chen, *Energy Environ. Sci.*, 2016, **9**, 357–390.

21 M. H. Seo, S. M. Choi, H. J. Kim and W. B. Kim, *Electrochem. Commun.*, 2011, **13**, 182–185.

22 M. Faraji, H. Gharibi and M. Javaheri, *J. Nanostruct.*, 2016, **6**, 154–164.

23 R. Kou, Y. Y. Shao, D. H. Wang, M. H. Engelhard, J. H. Kwak, J. Wang, V. V. Viswanathan, C. M. Wang, Y. H. Lin, Y. Wang, I. A. Aksay and J. Liu, *Electrochem. Commun.*, 2009, **11**, 954–957.

24 K.-W. Nam, J. Song, K.-H. Oh, M.-J. Choo, H. A. Park, J.-K. Park and J. W. Choi, *J. Solid State Electrochem.*, 2013, **17**, 767–774.

25 I.-Y. Jeon, D. H. Kweon, S.-W. Kim, S.-H. Shin, Y. K. Im, S.-Y. Yu, M. J. Ju and J.-B. Baek, *J. Mater. Chem. A*, 2017, **5**, 21936–21946.

26 J. W. Ma, A. Habrioux, Y. Luo, G. Ramos-Sánchez, L. Calvillo, G. Granozzi, P. B. Balbuena and N. Alonso-Vante, *J. Mater. Chem. A*, 2015, **3**, 11891–11904.

27 Z. Li, Q. Gao, H. Zhang, W. Tian, Y. Tan, W. Qian and Z. Liu, *Sci. Rep.*, 2017, **7**, 43352.

28 C. A. Campos-Roldán, G. Ramos-Sánchez, R. G. Gonzalez-Huerta, J. R. Vargas García, P. B. Balbuena and N. Alonso-Vante, *ACS Appl. Mater. Interfaces*, 2016, **8**, 23260–23269.

29 I. Hussainova, R. Ivanov, S. N. Stamatin, I. V. Anoshkin, E. M. Skou and A. G. Nasibulin, *Carbon*, 2015, **88**, 157–164.

30 C. Wang, L. Ma, L. Liao, S. Bai, R. Long, M. Zuo and Y. Xiong, *Sci. Rep.*, 2013, **3**, 2580.

31 Y. Shao, S. Zhang, C. Wang, Z. Nie, J. Liu, Y. Wang and Y. Lin, *J. Power Sources*, 2010, **195**, 4600–4605.

32 Y. Yu and B. Xu, *Acta Chim. Sin.*, 2003, **61**, 1758–1764.

33 W. A. Spieker, J. Liu, J. T. Miller, A. J. Kropf and J. R. Regalbuto, *Appl. Catal., A*, 2002, **232**, 219–235.

34 A. C. Ferrari and J. Robertson, *Phys. Rev. B: Condens. Matter Mater. Phys.*, 2000, **61**, 14095–14107.

35 M. A. Pimenta, G. Dresselhaus, M. S. Dresselhaus, L. G. Cancado, A. Jorio and R. Saito, *Phys. Chem. Chem. Phys.*, 2007, **9**, 1276–1291.

36 L. J. Pan, S. Ott, F. Dionigi and P. Strasser, *Curr. Opin. Electrochem.*, 2019, **18**, 61–71.

37 Y. Liu, L. Zhang, B. G. Willis and W. E. Mustain, *ACS Catal.*, 2015, **5**, 1560–1567.

38 E. I. Vovk, A. V. Kalinkin, M. Y. Smirnov, I. O. Klebovskii and V. I. Bukhtiyarov, *J. Phys. Chem. C*, 2017, **121**, 17297–17304.

39 S. N. Stamatin, I. Hussainova, R. Ivanov and P. E. Colavita, *ACS Catal.*, 2016, **6**, 5215–5221.

40 J. W. Ma, A. Habrioux, C. Morais, A. Lewera, W. Vogel, Y. Verde-Gomez, G. Ramos-Sánchez, P. B. Balbuena and N. Alonso-Vante, *ACS Catal.*, 2013, **3**, 1940–1950.

41 M. Arenz, K. J. J. Mayrhofer, V. Stamenkovic, B. B. Blizanac, T. Tomoyuki, P. N. Ross and N. M. Markovic, *J. Am. Chem. Soc.*, 2005, **127**, 6819–6829.

42 R. R. Adžić, J. Wang and B. M. Ocko, *Electrochim. Acta*, 1995, **40**, 83–89.

43 D. R. Lide, *CRC handbook of chemistry and physics*, CRC Press, Boca Raton, 2001.

44 G. V. Fortunato, F. de Lima and G. Maia, *J. Power Sources*, 2016, **302**, 247–258.

45 J. Liu, W. Li, R. Cheng, Q. Wu, J. Zhao, D. He and S. Mu, *Langmuir*, 2019, **35**, 2580–2586.

46 F. E. Sarac Oztuna, S. B. Barim, S. E. Bozbag, H. Yu, M. Aindow, U. Unal and C. Erkey, *Electrochim. Acta*, 2017, **250**, 174–184.

47 E. Teran-Salgado, D. Bahena-Uribe, P. A. Márquez-Aguilar, J. L. Reyes-Rodriguez, R. Cruz-Silva and O. Solorza-Feria, *Electrochim. Acta*, 2019, **298**, 172–185.

48 X. Tang, Y. Zeng, L. Cao, L. Yang, Z. Wang, D. Fang, Y. Gao, Z. Shao and B. Yi, *J. Mater. Chem. A*, 2018, **6**, 15074–15082.

49 Y. Zhou, X. Cheng, C. H. Yen, C. M. Wai, C. Wang, J. Yang and Y. Lin, *J. Power Sources*, 2017, **347**, 69–78.

50 K. Fu, Y. Wang, L. Mao, J. Jin, S. Yang and G. Li, *Electrochim. Acta*, 2016, **215**, 427–434.

51 A. Marinkas, R. Hempelmann, A. Heinzel, V. Peinecke, I. Radev and H. Natter, *J. Power Sources*, 2015, **295**, 79–91.

52 Y. J. Li, E. B. Zhu, T. McLouth, C. Y. Chiu, X. Q. Huang and Y. Huang, *J. Am. Chem. Soc.*, 2012, **134**, 12326–12329.

53 E. Bertin, A. Münzer, S. Reichenberger, R. Streubel, T. Vinnay, H. Wiggers, C. Schulz, S. Barcikowski and G. Marzun, *Appl. Surf. Sci.*, 2019, **467–468**, 1181–1186.

